The Microwave Detection of Wet Triacetone Triperoxide (TATP): Interplay Between Non-Covalent Forces and Water Dynamics

Susana Blanco[a], Alberto Macario[a], José García-Calvo[b], Andrea Revilla-Cuesta[b], Tomas Torroba[b], Juan Carlos López*[a]

[a] Prof. S. Blanco, Dr. A. Macario, Prof. J. C. López,
Departamento de Química Física y Química Inorgánica, Facultad de Ciencias, IU CINQUIMA, Universidad de Valladolid, 47011 Valladolid, Spain.
E-mail: sblanco@qf.uva.es, alberto.macario@uva.es, jclopez@qf.uva.es
[b] J. García-Calvo, A. Revilla-Cuesta, Prof. T. Torroba
Departamento de Química, Facultad de Ciencias, Universidad de Burgos, 09001 Burgos, Spain.
E-mail: jgcalvo@ubu.es, arcuesta@ubu.es, ttorroba@ubu.es

Supporting information for this article is given via a link at the end of the document.

Abstract: The water adducts of Triacetone triperoxide (TATP) have been observed using broadband rotational spectroscopy. This work opens a new way for the gas phase detection of this improvised explosive. The observed clusters exhibit unusual water dynamics and rarely observed multicenter interactions. TATP–H_2O is formed from the D_3 symmetry conformer of TATP with water lying close to the C_3 axis. Water rotation around this axis with a very low barrier gives rise to the rotational spectrum of a symmetric top. The main interaction of the monohydrate is a four-center trifurcated O_w-H···O hydrogen bond, not observed previously in the gas phase, reinforced by a weak four-center C-H···O_w interaction. Surprisingly all structural signatures show the weakness of these interactions. The complex TATP–$(H_2O)_2$ is formed from the monohydrated TATP by the self-association of water.

Introduction

Triacetone triperoxide ($C_9H_{18}O_6$, TATP, Scheme of Figure 1) forms part of the group of peroxide-based explosives that detonate following an entropy-driven process.[1] TATP could be used both as primary explosive and main charge[2] but its sensitivity and rapid sublimation discourage its use for commercial or military purposes. However, its ease of synthesis[1,2] and difficulty of detection[3,4] has made this compound to be a choice for the improvised explosive devices used by terrorists. Peroxide explosives have no aromaticity, nitro groups, or metallic elements so they are practically undetectable by direct UV-VIS absorption or fluorescence methods. Therefore, the need for rapid and highly selective detection methods for both prevention and forensic identification of these compounds has given rise to an intense activity of research on analytical methods. These include mass spectrometry techniques[2] and ion mobility spectrometry,[5] multiphoton electron extraction spectroscopy[6], or IR laser spectroscopy methods.[7] Portable and selective systems are still under development as those using fluorescence[8–10] and other types of sensors.[11–15] However, the signature of TATP is only clearly visible from bulky mass spectrometers.

One interesting property of TATP is its relatively high volatility, compared to other explosives, which makes it adequate for vapor detection[4] including gas-phase spectroscopic methods such as rotational spectroscopy. This includes a variety of techniques, which record the spectra associated with transitions between rotational states, which occur in the microwave (MW) region.

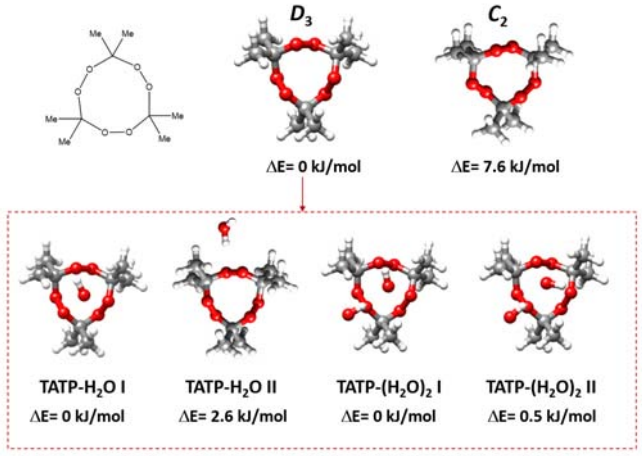

Figure 1. Scheme of triacetone triperoxide (TATP). The D_3 and C_2 symmetry conformers and the most stable complexes with water. DFT energies relative to the global minima are also given.

The application of this technique was mainly limited to stable molecular specimens of moderate size with a permanent dipole moment and possessing appreciable vapor pressures. However, the development of Fourier transform microwave (FTMW) spectroscopy in combination with supersonic-jet expansion techniques has contributed to overcome many of these drawbacks with reinforced high resolution and sensitivity.[16–19] Challenging molecular systems including a variety of weakly bound molecular complexes, in situ prepared unstable molecular species or solid biomolecules, generated by using electrical discharge or laser ablation respectively have been studied. The rotational spectra of very low dipole moment systems are now accessible, and the detection of molecules with zero dipole moment is possible if the molecule can form adducts with polar ligands as water.[20] Thus at present, FTMW spectroscopies can be considered as the most definitive gas-phase structural probes. They make possible the unambiguous discrimination between different isomers, also including tautomers, conformers, or isotopomers. The spatial mass distribution of such species have unique spectroscopic constants and distinct individual rotational

spectra, a key feature that makes these techniques to be powerful tools[21,22] in cases where other techniques may struggle.

The rotational study of TATP or any species related to it involves previous consideration of its structure to have reasonable sets of rotational constants and electric dipole moment components, which allow the prediction of the spectra. Previous experimental studies of TATP[23,24] have reported the existence of two conformers with D_3 and C_2 symmetries (Figure 1), the first having a 95% of abundance in solution at room temperature[24] and no dipole moment. For the second one, the electric dipole moment is close to zero. Although dipole moment in TATP is canceled by symmetry, it can be expected the having six oxygen atoms that can act as hydrogen bond (HB) acceptors the formation of complexes with polar molecules as water would render TATP accessible through FTMW spectroscopy. However, it has been reported that TATP oxygen atoms[1] can be encapsulated by their hydrophobic environment hindering the formation of the TATP microsolvates through OH··O HBs. In this context, we have explored the spectra of TATP in a supersonic jet using broadband CP-FTMW spectroscopy trying to observe their hydrated adducts. Their detection would additionally allow us to explore the structure and properties of this challenging and elusive system.

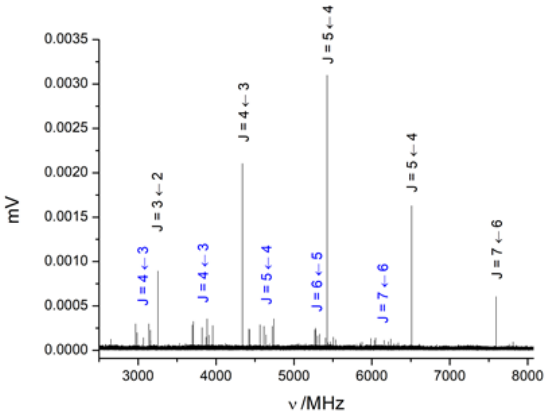

Figure 2. The rotational spectra observed for TATP with the assignments to TATP–H_2O (quantum numbers in black) and TATP–$(H_2O)_2$ (quantum numbers in blue) adducts.

Results and Discussion

Analysis of the Rotational spectrum

Before the investigation of the rotational spectrum of TATP exploration of the potential energy surfaces of TATP and its microsolvated clusters was done using theoretical methods to investigate the possible conformers, their relative energies, and their spectroscopic parameters. The complete exploration was done at B3LYP-GD3/6-311++G(2d,p) level. Additional calculations at the MP2/aug-cc-PVDZ level were done only for the most stable forms. The complete results are given in the supplementary information (see Tables S1-S4). The clusters with one or two water molecules and TATP in the D_3 and C_2 forms were explored. For the D_3 configuration, the two conformers shown in Figure 1 were found. In the global minimum, labeled TATP-H_2O I, water lies close to the C_3 axis of TATP with one of the O-H bonds practically aligned with this axis. In the second form, TATP-H_2O II, water approaches TATP from a side perpendicularly to the C_3 axis. Structurally similar adducts formed from the monomer in the C_2 form were found to have much higher energies (9-10 kJ/mol). For the dihydrated TATP adducts, the DFT calculations predict that the most stable clusters, shown in Figure 1, were those formed from the most stable monohydrated cluster by self-association of water. The cluster with both water molecules lying close to the C_3 axis on opposite sides of TATP was found to be 8.3 kJ/mol higher in energy. The most stable conformers found for the mono and dihydrated clusters were predicted to have reasonably high electric dipole moments.

In this work, we have explored the rotational spectrum of TATP using broadband chirped-pulse FTMW (CP-FTMW) spectroscopy. The spectrum taken directly from the sample of TATP is shown in Figure 2. The most prominent line series, observable without any water vapor addition, corresponds to the K = 0 lines of the successive J+1 ← J transitions of a symmetric top. No lines corresponding to other K values were observed. According to this assignment, the observed frequencies fit to the simple equation:

$$\nu_{J+1\leftarrow J} = 2B(J+1) - 4D_J\,(J+1)2 \qquad (1)$$

From which the rotational constant B and the centrifugal distortion constant D_J given in Table 1 were easily obtained.

Table 1. The rotational parameters of all the observed isotopologues of TATP–H_2O adduct (see Figures 3 and 4 for atom labeling)

Symmetric top	B/MHz[a]	D_J/kHz	n	σ/kHz
$C_9H_{18}O_6$–H_2O	542.471250(21)	0.01760(17)	7	0.5
$C_9H_{18}O_6$–$H_2{}^{18}O_w$	531.637511(24)[b]	[0.0176][c]	6	0.9
$C_9H_{18}O_6$–$D_{w1}OH$	540.097110(90)	[0.0176]	5	1.9
$C_9H_{18}O_6$–HOD_{w2}	535.69889(23)	[0.0176]	5	4.9
$C_9H_{18}O_6$–D_2O	533.41875(16)	[0.0176]	5	3.3
$C_9D_{18}O_6$–HOH	473.22611(54)	[0.0176]	5	4.0
Asymmetric top	**$^{13}C_1$-TATP–H_2O**	**$^{13}C_{10}$-TATP–H_2O**	**$^{13}C_{11}$-TATP–H_2O**	
A/MHz[a]	542.44647(21)	541.99307(17)	541.29217(26)	
B/MHz	540.19971(24)	537.24291(20)	536.68841(29)	
C/MHz	438.765(66)	437.081(15)	437.174(23)	
D_J/kHz	0.0173(22)	0.0188(18)	0.0163(27)	
D_K/kHz	0.0326(52)	0.0473(41)	0.0304(64)	
n	24	20	22	
σ/kHz	4.2	2.0	3.6	
P_{aa} /uÅ	577.848(87)	582.252(22)	582.011(31)	
P_{bb} /uÅ	573.974(87)[d]	574.007(22)	574.002(31)	
P_{cc} /uÅ	357.693(87)	358.438(22)	359.651(31)	

[a] A, B, and C are the determinable rotational constants. D_J and D_K are centrifugal distortion constants. n is the number of lines observed. σ is the rms deviation of the fit. $P_{\alpha\alpha}$ (α= a, b or c) is the planar moments of inertia derived from the moments of inertia Iα, as $P_{bb}=(I_a-I_b+I_c)/2$. [b] Standard errors in parenthesis are given in units of the last digit. [c] Constants in square brackets fixed to the parent species values. [d] The C rotational constant of the parent species can be estimated as 440.24(2) MHz from the ^{13}C rotational spectra planar moments P_{bb} ($I_c=2P_{bb}(^{13}C)-I_a+I_b \approx 2P_{bb}(^{13}C)$).

The most stable form of TATP is an asymmetric top but has no dipole moment. The experimental value of B = 542.471250(21) MHz is far from the value calculated for bare TATP, which is a symmetric top with a B rotational constants predicted to be close to 675 MHz. However, the experimental B value is comparable to those calculated at different levels for the most stable conformer of the complex TATP–H2O I that are listed in Figure 3. In this complex, TATP is in its D_3 configuration and water lies close to the C_3 symmetry axis, which in turn is coincident with

the *c* principal inertial axis of TATP. The theoretical equilibrium structure corresponds to a near-oblate asymmetric rotor with slightly different A and B rotational constants (see Figure 3). The identification of the observed symmetric rotor species with the predicted TATP–H_2O I complex is thus only possible by assuming that water is almost freely rotating around the TATP *c* axis (see Figure 3). Relaxed scans, done to explore the energy profile of TATP–H_2O for the rotation of water around the C_3 symmetry axis, give a three-fold periodic potential energy function with three equivalent conformations and barriers close to 200 cm^{-1} that can be seen in Figure 3. Using a three-fold periodic function, the flexible model of Meyer[25] shows that for a wide range of barrier values, the rotational constants of the ground vibrational state average to those of a symmetric top as summarized in Figure 3. Besides the μ_a and μ_b electric dipole moment average to zero and only μ_c is different from zero in good agreement with the experimental observations. Thus, under this dynamical perspective, the complex TATP-water can be considered as an effective C_3 symmetry species behaving as an effective symmetric rotor.

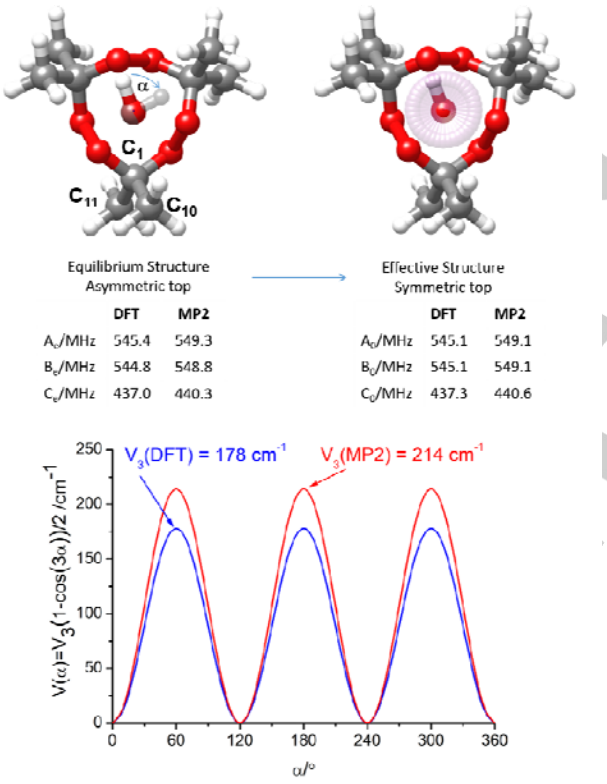

Figure 3. The predicted B3LYP–D3/6-311++G(2d,p) (DFT) and MP2/aug-cc-pVDZ (MP2) three-fold periodic potential energy functions for the internal rotation of water around the bonded O-H bond, described by the angle α. For such a water rotation it can be shown (see text) that the effective ground state rotational constants of TATP–H_2O average to those of a symmetric top.

This identification of the TATP-H_2O conformer was confirmed from successive experiments using isotopically enriched samples as $C_9H_{18}O_6$–$H_2{}^{18}O$, $C_9H_{18}O_6$–$D_{w1}OH$, $C_9H_{18}O_6$–HOD_{w2}, $C_9H_{18}O_6$–D_2O and $C_9D^{18}O_6$–H_2O, all of them behaving as symmetric rotors. On the other hand, the ^{13}C isotopologues are expected to be slightly asymmetric tops spectra.[26] For an effective C_3 symmetry, there are only three different monosubstituted ^{13}C isotopologues which were observed in their natural abundance. The rotational parameters of all these isotopologues are given in Table 1. The observed planar inertial moments of the ^{13}C isotopologues ($2P_{bb} \approx I_c$) allow estimating the C rotational constant for TATP–H_2O as C = 440.24(2) MHz in good agreement with the value calculated at MP2/aug-cc-pVDZ level (see Figure 3).

Table 2. The observed rotational parameters of TATP–$(H_2O)_2$ compared to those calculated at B3LYP-D3/6-311++G(2d,p) (DFT) and MP2/aug-cc-pVDZ (MP2) levels of theory for the most stable forms.

Parameter [a]	Exp.	DFT	MP2
A/MHz	507.53454 (52)[b]	506.2	510.90
B/MHz	407.351859(85)	415.8	417.26
C/MHz	362.044078(94)	367.1	368.13
D_J/kHz	0.01353(47)		
$\lvert\mu_a\rvert/\lvert\mu_b\rvert/\lvert\mu_c\rvert$/D	+ / - / -	4.0/1.0/1.6	4.0/1.0/1.4
n	81		
σ	3.6		

[a] *A*, *B* and *C* are the rotational constants. D_J is a centrifugal distortion constant. μ_a, μ_b and μ_c are the electric dipole moment components (in Debye); (+) or (-) reflect the selection rules observed. n is the number of measured lines. σ is the rms deviation of the fit. [b] Standard errors are given in parenthesis in units of the last digit.

A weaker asymmetric rotor spectrum (see Figure 2) consisting of groups of evenly spaced μ_a-type R-branch transitions was also assigned. The rotational lines were analyzed using the semirigid rotor Hamiltonian of Watson[27] The corresponding rotational constants given in Table 2 are comparable to those calculated for the three most stable forms of TATP–$(H_2O)_2$. The observation of the spectra of the $C_9H_{18}O$–$H_2{}^{18}O$–H_2O, $C_9H_{18}O$–H_2O–$H_2{}^{18}O$, $C_9H_{18}O$–DOH–H_2O, $C_9H_{18}O_6$–H_2O–DOH and $C_9H_{18}O_6$–DOH–DOH isotopologues (see Table S5) confirms the identification of the spectrum as either one of the two most stable forms TATP–$(H_2O)_2$ I or TATP–$(H_2O)_2$ II. A relaxed scan over the rotation of the central water molecule around the C_3 axis of TATP predicts a barrier to interconversion between these conformers of 138 cm^{-1} (see Figure S3) A collisional relaxation process in the supersonic jet, allowed by a barrier < 400 cm-1,[28] could explain the observation of only the most stable form, assumed from now on to be TATP–$(H_2O)_2$ I. All the measured frequencies for both TATP-H_2O and TATP-$(H_2O)_2$ are given in the Supplementary Information, Tables S13-S16.

Structure

The r_s substitution method of Kraitchman[29,30] is a purely experimental approach that allows us to locate directly the substituted atoms of a molecule or adduct. It gives the absolute values of the substituted atom coordinates in the principal inertial axis system of the parent molecule. The signs of the coordinates can be taken from a reasonable molecular structure. Multi-isotopic information can be also used to get an effective ground state r_0 structure. Bond distances and angles are in this case obtained from a least-squares fit of all of the available rotational parameters.[31]

For TATP–H_2O the effective C_3 symmetry reduces the determinable structural parameters to only the *c* coordinates for

water atoms. Thereby, the high symmetry also reduces the number of independent structural parameters of TATP,[26] there are only two distinct C-C or C-O bonds and two different methyl groups. The r_s *c* coordinates of the water atoms calculated from the I_b inertial moments from Kraitchman equations[29,30] are given in Figure 4. Using these coordinates we have subtracted the inertial contributions[32] of water atoms to obtain the rotational constant of bare TATP which are compared in Table 3 with those calculated from the theoretical and r_0 structures of TATP-H_2O. These constants are better reproduced by the MP2/aug-cc-pVDZ structure so we have used it as initial in the determination of the r_0 structure of TATP–H_2O.

As has been demonstrated for high-symmetry molecular species, a relatively small number of measured isotopologues makes not prohibitive the determination of a reliable molecular geometry if molecular symmetry is considered. In the case of TATP-H_2O, the C_3 effective symmetry can be taken into account by declaring the parameters associated with the different C, O, and H atoms in a centrosymmetric way as shown in Figure S1. Besides, the projection of the non-bonded H_{w2} atom on the *c* axis has been considered instead of its real position. However, even with those simplifications, several parameters ought to be kept fixed. These parameters, including those associated with the C–H bonds, were fixed to the MP2/aug-cc-pVDZ equilibrium structure values. A least-squares fit of all the available experimental constants was done. The fitted centrosymmetric parameters were then converted into the chemically relevant structural parameters. The structural parameters associated with the location of water in TATP-H_2O are summarized in Figure 4. All the fixed and fitted centrosymmetric parameters as well as the bond distances and angles are listed and compared to the theoretical structures for the most stable TATP–H_2O I in Table S7. Tables S6-S8 collect all the structural results and compare them to the theoretical structures and the X-ray structure of the monomer.[1]

Table 3. Results of the estimation of the rotational constants of bare TATP reflecting the structure of this molecule in the observed TATP–H_2O complex.

	Exp.	DFT	MP2	r_0
A/MHz	674.46(5) [a,b]	672.9	675.7	674.41
B/MHz	674.46(5)	672.9	675.7	674.41
C/MHz	440.24(2)[c]	437.3	440.7	440.18

[a] *A* or *B* rotational constants for the monomer estimated by subtracting the inertial contribution of water atoms in the monohydrated complex from the r_s coordinates (see Table S6). [b] Estimated or standard errors in parenthesis are given in units of the last digit. [c] Estimated from the planar moments P_{bb} of ^{13}C species of TATP-H_2O by assuming very small changes upon complexation.

From both the r_s and r_0 data one could expect that water location in TATP–H_2O is reliable. However, the determination of the position of hydrogen atoms, expected to be more affected than oxygen by water dynamics, deserves some discussion. The difference of 0.338(1) Å between the r_s *c* components of the non-bonded hydrogen atom H_{w2} and the O_w atom of water suggest a precession of the bonding O_w-H_{w1} bond around the C_3 symmetry. A small precession angle of 6° can be estimated by assuming that the HOH atom of water is not altered upon complexation (see Figure 4). The $r_s(O_w\text{-}H_{w1})$ distance of 1.069(1) Å is somewhat large considering the standard r_0(O-H)=0.965 Å of water[33] even if this bond might be enlarged by hydrogen bonding. However, there is no indication from theoretical calculations for appreciable lengthening of this bond on complexation. Thus, some shortening of the $r_0(O_w\cdots x_1)$ distance from the water oxygen atom to the TATP center of mass, at point x_1 (see Figure 4), due to the Ubbelohde effect[34] would be expected. A shortening value of $\Delta r(O_w\cdots x_1)$= –3.7 mÅ is calculated from the simple expression:

$$\Delta B_{obs} - \Delta B_{calc} = (\partial B/\partial r(O_w\cdots x_1))\,\Delta r(O_w\cdots x_1) \quad (2)$$

This suggests the existence of an incipient Ubbelodhe effect of the same magnitude as those found in weak hydrogen-bonded systems.[35]

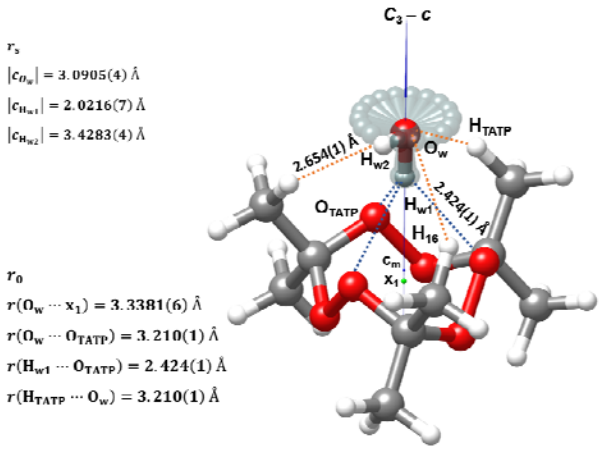

Figure 4. r_0 structure of TATP–H_2O. x_1 is the intersection point between the C_3 axis and the central CCC plane.

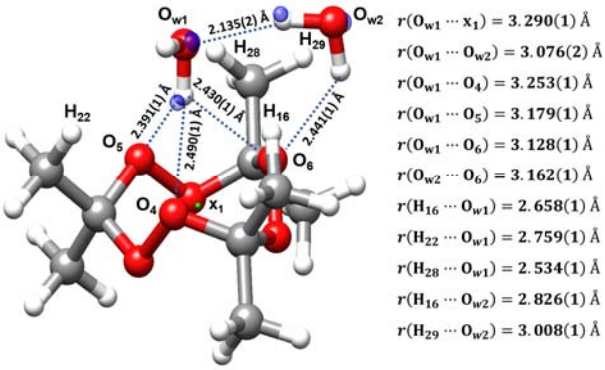

Figure 5. The r_s positions (in blue) for the O and H atoms of water molecules are compared to the r_0 structure of TATP– $(H_2O)_2$. A summary of the r_0 hydrogen bond distances is given

The investigation of the structure of the complex TATP-$(H_2O)_2$ was done following the same procedures as done for TATP-H_2O A partial r_0 structure to locate the water molecules in the complex was determined by fixing the parameters of TATP to those determined for the TATP-H_2O complex. The results of the structural investigation are summarized in Figure 5. The complete results are given in Figure S2 and Tables S9-S11 where they are compared to the theoretical equilibrium structures for the predicted global minimum. The derived partial

r_0 structure of TATP–$(H_2O)_2$ (Figure 5) shows it as formed from TATP–H_2O with the second water acting as a double proton donor to the first water molecule and the closest endocyclic TATP oxygen atom. The $O_w\cdots O_{TATP}$ TATP–$(H_2O)_2$ intermolecular distances are similar to those found in the heterodimer. However, the r_0 distance ($r(O_{w1}\cdots O_{w2})$ = 3.076 Å) between water oxygen atoms is closer to the standard O-H···O distance (2.976 Å for water dimer)[36] indicating that this is the strongest HB in the complex. The distances between water oxygen atoms and the closest methyl group hydrogen atoms suggest also the existence of five weak C-H···O_w HB. (see Figure 5)

Nature of the intermolecular interactions

Based on the observed structure (see Figure 4), the main TATP–H_2O interaction can be described as a trifurcated O-H···O hydrogen bond (HB) from water to the closest endocyclic TATP oxygen atoms. According to the literature, it is a four-center bond with three acceptor groups.[37] Trifurcated interactions are rarely observed in crystal structures and this is probably one of the first cases for which this interaction is observed in the gas phase. The experimental HB distances are larger than the values expected for a conventional O-H···O HB, ($r(O_w\cdots O_{TATP})$ = 3.210(1) Å *vs.* 2.976 Å for water dimer).[36] This is an indication of the weakness of the O-H··O HBs in TATP–H_2O. The distances $r_0(H_{TATP}\cdots O_w)$ = 2.654(1) Å from the neighbor H atoms of TATP to the water oxygen atom indicate the existence of three additional C-H···O HB weak contacts,[38,39] which, according to the literature, could be considered as four-center chelated weak HBs.[37] These weak HBs, breaking as water rotates around the C_3 axis, underpin the calculated three-fold barrier for water rotation which averages to produce an effective symmetric top (see Figure 3).

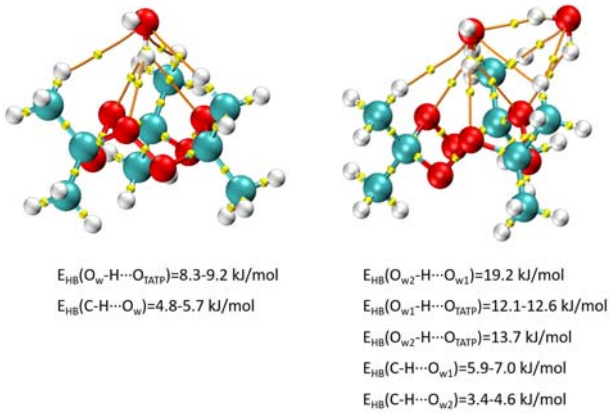

Figure 6. Bond critical points (yellow) and bond paths (orange) calculated for TATP–H_2O and TATP–$(H_2O)_2$. The figure gives the ranges of the estimated interaction energies from the electron potential density $V(r)$ calculated at the BCPs.

Additional information to confirm the number and nature of the hydrogen bond interactions in both complexes can be derived from the Quantum Theory of "atoms in molecules" (QTAIM)[40,41] analysis. Figure 6 shows the calculated bond paths (BPs) and the (3,-1) bond critical points (BCPs) indicating the formation of bonds for TATP-H_2O (left) and TATP-$(H_2O)_2$ (right) calculated for both the mono and dihydrated clusters at MP2/aug-cc-pVDZ level. The BPs and BCPs confirm the existence in TATP-H_2O of a trifurcated O-H···O hydrogen bond (HB) established from water to the closest endocyclic TATP oxygen atoms. The stability of the complex is reinforced by the three additional C-H···O HB weak contacts from the neighbor H atoms of TATP to the water oxygen atom, already mentioned. In TATP-$(H_2O)_2$ the water molecule on top of TATP, close to the C_3 axis, has the same BPs and BCPs, that is, the same interactions with TATP as in TATP-H_2O. The second water molecule shows two BPs and the corresponding BCPs showing O-H···O hydrogen bond interactions to the first water molecule and the closest TATP oxygen atom. Besides, two BPs and two BCPs draw two weak C-H···O_{w2} interactions. Estimation of the interaction energies from the electron potential density $V(r)$ calculated at the BCPs gave the values listed in Figure 6. These correspond to weak interactions if we consider weak hydrogen bonds those with energies smaller than 16.7 kJ/mol (4 kcal/mol).[37] The exception is the O_{w2}–H···O_{w1} HB in TATP–$(H_2O)_2$.

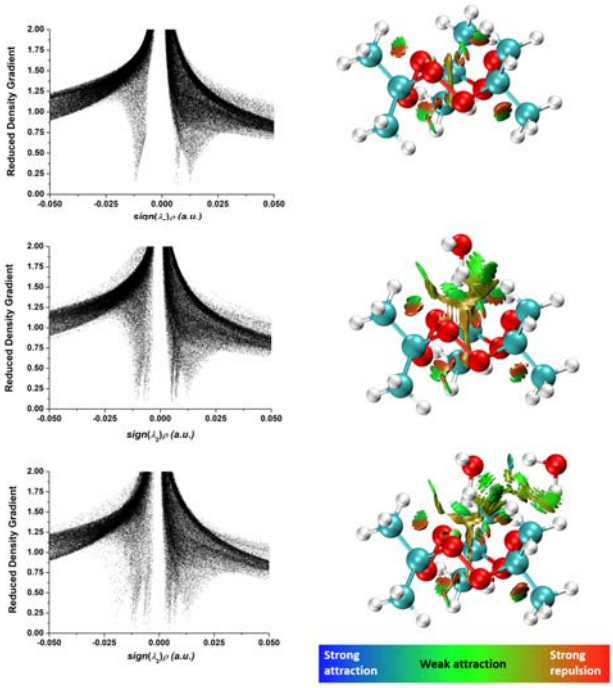

Figure 7. Results of the non-covalent interaction (NCI) analysis[42] done for TATP, TATP-H_2O and TATP-$(H_2O)_2$. Each point in the scatter graphs corresponds to a grid point in 3D space and represents the reduced density gradient (RDG) *vs.* sign[$\lambda_2(\mathbf{r})$]$\rho(\mathbf{r})$. The spikes on the left (negative side) correspond to attractive interactions. Those on the right side correspond to repulsive interactions. The points corresponding to low RDG values represent weak interactions. Those with RGD<0.5 a.u. are represented in the isosurface.

Non-covalent interaction (NCI) analyses[42] were also done to visualize the interactions present in the TATP monomer and in the adducts. The results are illustrated in Figure 7. In the scatter graphs the *y* and *x* axis represent the reduced density gradient (RDG) and the sign[$\lambda_2(\mathbf{r})$]$\rho(\mathbf{r})$ functions. Each point in this graph corresponds to a point in 3D-space. $\lambda_2(\mathbf{r})$ is the largest second eigenvalue of the Hessian matrix of the electron density $\rho(\mathbf{r})$. The strength of weak interactions has a positive correlation with

the electron density in the corresponding region; van der Waals interaction regions always have very small values of ρ, while the regions corresponding to strong steric effects and hydrogen bonding always have relatively large values of ρ. A negative sign of $\lambda_2(\mathbf{r})$ indicates attractive interactions since electron density is aggregated as in (3,-1) bond critical points. A positive sign indicates repulsive interactions in which the electron density depletes. Thus, the product of the sign of $\lambda_2(\mathbf{r})$ and $\rho(\mathbf{r})$ allows visualizing the non-covalent interactions. The spikes in the low part of the scatter graphs represent the non-covalent interactions present. Those on the left part of the graph correspond to attractive interaction and those on the right part correspond to repulsive interactions. The isosurfaces on the right give the points with RDG>0.5. The attractive or repulsive character and the strength of the interactions are shown in the isosurface representation using a color code. The TATP monomer shows a series of attractive weak H···O and repulsive O···O, C···O interactions and steric effects. The number of spikes in the graph for both attractive and repulsive parts increase in TATP-H_2O and the isosurface shows the multiple interactions regions corresponding to the trifurcated O_w-H···O_{TATP} four-center bond interactions and the chelated four-center C-H···O_w interactions already discussed. However the color codes and the values of sign[$\lambda_2(\mathbf{r})$]$\rho(\mathbf{r})$ show that these attractive interactions are weak. Repulsive interactions and steric effects between water and TATP also appear and might hinder the approach of water to TATP to give shorter O_w-H···O distances and stronger hydrogen bonds. In TATP-$(H_2O)_2$ the number of spikes is still increasing, but in this case, only the O_{w2}-H···O_w proves to correspond to be a standard moderate hydrogen bond. Figures S4 and S5 show the combined results of QTAIM and NCI analyses where the coincidence of (3,–1) BCP and NCI attractive regions is evident.

Dissociation energy and cooperativity effects

The dissociation energy of TATP–H_2O has been calculated to be 7 kJ/mol from the D_J centrifugal distortion constant and the pseudodiatomic model[43] by assuming a Lennard-Jones potential for the stretching intermolecular vibration (see Table S 12). This energy is ~1/3 of the value of 22.5 kJ/mol calculated from BSSE corrected counterpoise calculations and this might indicate this pseudodiatomic model is no appropriate for this system. The corresponding dissociation energy of TATP–$(H_2O)_2$ is calculated in the same way as 50.5 kJ/mol more than two-times the predicted value for the heterodimer. This indicates some contribution of cooperative effects if we take into account the predicted dissociation energy of water dimer at the same level of 18.7 kJ/mol. The role of cooperative effects is shown when observing some shortening of the O_{w1}-O_{TATP} distances (see Figures 4 and 5) and the increase of the interaction energies estimated from the electron potential density $V(r)$ calculated at the BCPs in going from TATP–H_2O to TATP–$(H_2O)_2$ (see Figure 6). The energies of the O_w-H···O_{TATP} and C-H···O_w interactions with the central water molecule increase notably in going from both TATP–H_2O to TATP–$(H_2O)_2$.

Conclusion

To summarize, we have shown here that TATP can be detected in the gas phase from rotational spectroscopy by using its hydrated adducts as spectroscopic targets. These are observed even without adding water to the sample. Interestingly the TATP–H_2O complex is an effective symmetric top due to the internal rotation of water. We have also shown from the study of deuterated water isotopologues that this complex show an incipient Ubbelohde effect.[34] The mono and dihydrated TATP adducts show complex networks of weak O_w-H···O and C-H···O_w HBs. The main TATP-H_2O interaction is a rarely observed four-center trifurcated O_w-H···O interaction. This interaction proves to be weak, with distances larger than expected even if the contribution of the TATP oxygen atoms gives rise to regions of high electron density around the C_3 axis. It has been reported that TATP oxygen atoms are encapsulated by the hydrocarbon environment.[1] Instead, we have observed that the methyl groups interact with water through attractive weak C-H···O_w four-center chelated interactions which break and form as water rotates giving rise to a small three-fold barrier for water rotation. Here we show from an NCI that TATP and water apart from attractive interactions suffer repulsive and steric interactions that limit the distance at what water may approach to the oxygen atoms The structure of TATP in the complexes also reveals other interesting features. The predicted O-O and C-O bond distances, involved in explosion reactions,[1] are calculated to increase by about 0.01 Å upon complexation, so probably the interaction with water destabilizes TATP.

TATP can form complexes with ions[11] but it shows notable differences with other macrocycles as crown ethers.[20,44] Our results show that TATP is rather rigid while crown ethers are so flexible that easily change their conformation upon complexation with water.[20,44] The intermolecular O-H···O HB's are moderately strong in crown ether-water adducts but these are weak in TATP-water complexes.

Experimental Section

Exploration of the potential energy surfaces of TATP, TATP–H_2O, and TATP–$(H_2O)_2$ was done using Gaussian 16.[45] DFT calculations at the B3LYP/6-311++G(2d,p) using D3 Grimme´s dispersion correction[46] were done in a first step to finding the possible conformers of these species. In a second step, calculations at the MP2/aug-cc-pVDZ level were done only for the most stable conformers. The results including energies, rotational parameters, and electric dipole moments are given in Tables S1-S4. Complexation E_{BSSE} energies were calculated taking into account basis set superposition error (BSSE).[47] Relaxed scans were done to explore the energy profile of TATP–H_2O for the rotation of water around the bonded O–H and for TATP–$(H_2O)_2$ to explore the interconversion between the two most stable conformers I and II. The interactions responsible for the formation of the complexes have been further investigated at the MP2/aug-cc-pVDZ level through Quantum Theory of "atoms in molecules" (QTAIM)[40,41] and a non-covalent interaction (NCI) analysis[42] using Multiwfn.[41]

All TATP samples were synthesized from acetone and hydrogen peroxide under acidic catalysis following reported procedures.[2,8,9] Commercial samples of $H_2{}^{18}O$ and D_2O were also used. The rotational spectrum of TATP–H_2O has been recorded in the 2-10 GHz frequency region using a chirped-pulse Fourier transform microwave spectrometer (CP-FTMW)[48] that follows Pate´s[49] design. The carrier gas used was Ne at stagnation pressures of 2 bar. It was expanded through a 0.8 mm nozzle in pulses of 700 μs. In each experiment, a small amount (< 0.2 g) of TATP (m. p. ~ 98°C) was placed in a reservoir incorporated in the

heatable nozzle and gently heated up to a maximum of 45°C. A deposit with water inserted in the gas line allowed the previous mixing of the water vapor with the carrier gas. Chirp pulses of 4 μs were created by an arbitrary waveform generator and amplified to 20 W. This polarization power limits the optimum chirp bandwidth to a maximum value of 2 GHz, so the complete spectrum is usually recorded in several steps. The polarization signal was radiated from a horn antenna in a direction perpendicular to that of the expanding gas. A molecular transient emission spanning 40 μs is then detected through a second horn, recorded with a digital oscilloscope and Fourier-transformed to the frequency domain. The accuracy of frequency measurements is better than 15 kHz. Tables S13-S16 collect all measured frequencies.

Acknowledgments

SB, AM, and JCL acknowledge the Ministerio de Economía y Competitividad (Grant CTQ2016-75253-P) for financial support. JGC, ARC and TT acknowledge the NATO Science for Peace and Security Programme (Grant SPS G5536), the Junta de Castilla y León, Consejería de Educación y Cultura y Fondo Social Europeo (Grant BU263P18) and the Ministerio de Ciencia e Innovación (Grant PID2019-111215RB-100) for financial support.

References

[1] F. Dubnikova, R. Kosloff, J. Almog, Y. Zeiri, R. Boese, H. Itzhaky, A. Alt, E. Keinan, *J. Am. Chem. Soc.* **2005**, *127*, 1146–1159.

[2] M. Mäkinen, M. Nousiainen, M. Sillanpää, *Mass Spectrom. Rev.* **2011**, *30*, 940–973.

[3] S. Giannoukos, B. Brkić, S. Taylor, A. Marshall, G. F. Verbeck, *Chem. Rev.* **2016**, *116*, 8146–8172.

[4] D. S. Moore, *Rev. Sci. Instrum.* **2004**, *75*, 2499–2512.

[5] D. Jiang, L. Peng, M. Wen, Q. Zhou, C. Chen, X. Wang, W. Chen, H. Li, *Anal. Chem.* **2016**, *88*, 4391–4399.

[6] S. Tang, N. Vinerot, D. Fisher, V. Bulatov, Y. Yavetz-Chen, I. Schechter, *Talanta* **2016**, *155*, 235–244.

[7] J. S. Li, B. Yu, H. Fischer, W. Chen, A. P. Yalin, *Rev. Sci. Instrum.* **2015**, *86*, 031501.

[8] J. García-Calvo, P. Calvo-Gredilla, M. Ibáñez-Llorente, D. C. Romero, J. V. Cuevas, G. García-Herbosa, M. Avella, T. Torroba, *J. Mater. Chem. A* **2018**, *6*, 4416–4423.

[9] P. Calvo-Gredilla, J. García-Calvo, J. V. Cuevas, T. Torroba, J.-L. Pablos, F. C. García, J.-M. García, N. Zink-Lorre, E. Font-Sanchis, Á. Sastre-Santos, et al., *Chem. Eur. J.* **2017**, *23*, 13973–13979.

[10] M. R. Rao, Y. Fang, S. De Feyter, D. F. Perepichka, *J. Am. Chem. Soc.* **2017**, *139*, 2421–2427.

[11] F. Dubnikova, R. Kosloff, Y. Zeiri, Z. Karpas, J. Almog, Y. Zeiri, R. Boese, H. Itzhaky, A. Alt, E. Keinan, *J. Phys. Chem. A* **2002**, *106*, 4951–4956.

[12] A. Lichtenstein, E. Havivi, R. Shacham, E. Hahamy, R. Leibovich, A. Pevzner, V. Krivitsky, G. Davivi, I. Presman, R. Elnathan, et al., *Nat. Commun.* **2014**, *5*, 4195.

[13] Q. Sun, Z. Wu, H. Duan, D. Jia, Q. Sun, Z. Wu, H. Duan, D. Jia, *Sensors* **2019**, *19*, 1281.

[14] A. Üzer, S. Durmazel, E. Erçağ, R. Apak, *Sensors Actuators B Chem.* **2017**, *247*, 98–107.

[15] B. A. G. Hammer, K. Müllen, *Chem. Rev.* **2016**, *116*, 2103–2140.

[16] J.-U. Grabow, W. Caminati, *Front. Mol. Spectrosc.* **2009**, 383–454.

[17] B. H. Pate, *Science* **2011**, *333*, 947–948.

[18] A. L. Christophe, J. T. Barnes, S. Twagirayezu, A. Mikhonin, M. T. Muckle, J. L. Neill, *Appl. Spectrosc.* **2019**, *73*, 1334–1339.

[19] D. W. Armstrong, M. Talebi, N. Thakur, M. F. Wahab, A. V. Mikhonin, M. T. Muckle, J. L. Neill, *Angew. Chemie Int. Ed.* **2020**, *59*, 192–196.

[20] C. Pérez, J. C. López, S. Blanco, M. Schnell, *J. Phys. Chem. Lett.* **2016**, *7*, 4053–4058.

[21] S. Blanco, M. E. Sanz, J. C. López, J. L. Alonso, *Proc. Natl. Acad. Sci. U. S. A.* **2007**, *104*, 20183–20188.

[22] A. Macario, S. Blanco, J. Thomas, Y. Xu, J. C. López, *Chem. Eur. J.* **2019**, *25*, 12325–12331.

[23] C. Denekamp, L. Gottlieb, T. Tamiri, A. Tsoglin, R. Shilav, M. Kapon, *Org. Lett.* **2005**, *7*, 2461–2464.

[24] N. Haroune, A. Crowson, B. Campbell, *Sci. Justice* **2011**, *51*, 50–56.

[25] R. Meyer, *J. Mol. Spectrosc.* **1979**, *76*, 266–300.

[26] C. Pérez, A. L. Steber, A. M. Rijs, B. Temelso, G. C. Shields, J. C. Lopez, Z. Kisiel, M. Schnell, *Phys. Chem. Chem. Phys.* **2017**, *19*, 14214–14223.

[27] J. K. G. Watson, in *Vib. Spectra Struct. a Ser. Adv. Vol 6* (Ed.: J.R. Durig), Elsevier, New York, **1977**, pp. 1–89.

[28] R. S. Ruoff, T. D. Klots, T. Emilsson, H. S. Gutowsky, *J. Chem. Phys.* **1990**, *93*, 3142–3150.

[29] J. Kraitchman, *Am. J. Phys.* **1953**, *21*, 17–24.

[30] B. P. van Eijck, *J. Mol. Spectrosc.* **1982**, *91*, 348–362.

[31] Z. Kisiel, *J. Mol. Spectrosc.* **2003**, *218*, 58–67.

[32] J. C. Lopez, R. Sanchez, S. Blanco, J. L. Alonso, *Phys. Chem. Chem. Phys.* **2015**, *17*, 2054–2066.

[33] M. D. Harmony, V. W. Laurie, R. L. Kuczkowski, R. H. Schwendeman, D. A. Ramsay, F. J. Lovas, W. J. Lafferty, A. G. Maki, *J. Phys. Chem. Ref. Data* **1979**, *8*, 619.

[34] A. R. Ubbelohde, K. J. Gallagher, IUCr, *Acta Crystallogr.* **1955**, *8*, 71–83.

[35] Q. Gou, G. Feng, L. Evangelisti, D. Loru, J. L. Alonso, J. C. López, W. Caminati, *J. Phys. Chem. A* **2013**, *117*, 13531–13534.

[36] J. A. Odutola, T. R. Dyke, *J. Chem. Phys.* **1980**, *72*, 5062–5070.

[37] G. A. Jeffrey, *An Introduction to Hydrogen Bonding*, Oxford University Press, **1997**.

[38] T. Steiner, *Chem. Commun.* **1997**, 727–734.

[39] G. R. (Gautam R. . Desiraju, T. Steiner, *The Weak Hydrogen Bond : In Structural Chemistry and Biology*, Oxford University Press, **2001**.

[40] R. F. W. Bader, *Chem. Rev.* **1991**, *91*, 893–928.

[41] T. Lu, F. Chen, *J. Comput. Chem.* **2012**, *33*, 580–592.

[42] E. R. Johnson, S. Keinan, P. Mori-Sánchez, J. Contreras-García, A. J. Cohen, W. Yang, *J. Am. Chem. Soc.* **2010**, *132*, 6498–6506.

[43] D. J. Millen, *Can. J. Chem.* **1985**, *63*, 1477–1479.

[44] J. C. López, C. Pérez, S. Blanco, V. A. Shubert, B. Temelso, G. C. Shields, M. Schnell, *Phys. Chem. Chem. Phys.* **2019**, *21*, 2875–2881.

[45] M. J. et al Frisch, *Gaussian16, rev. A.03, Gaussian Inc., Wallingford, CT,* **2016**.

[46] S. Grimme, *Wiley Interdiscip. Rev. Comput. Mol. Sci.* **2011**, *1*, 211–228.

[47] S. F. Boys, F. Bernardi, *Mol. Phys.* **1970**, *19*, 553–566.

[48] P. Pinacho, S. Blanco, J. C. López, *Phys. Chem. Chem. Phys.* **2019**, *21*, 2177–2185.

[49] G. G. Brown, B. C. Dian, K. O. Douglass, S. M. Geyer, S. T. Shipman, B. H. Pate, *Rev. Sci. Instrum.* **2008**, *79*, 4–5.

Entry for the Table of Contents

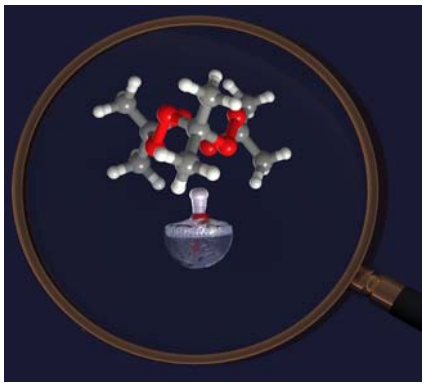

Wetting triacetone triperoxide (TATP) makes possible the rotational detection of this non-polar explosive through TATP-H_2O and TATP-$(H_2O)_2$ adducts. The dynamics of water in the TATP–H_2O converts it in a symmetric top. The main interaction is a four center trifurcated O_w-H···O hydrogen bond, not observed previously in the gas phase. Structural signatures and theoretical calculations show the weakness of the interactions between water and TATP.

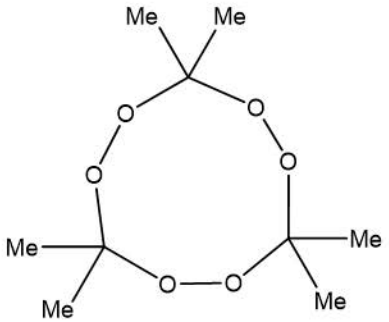

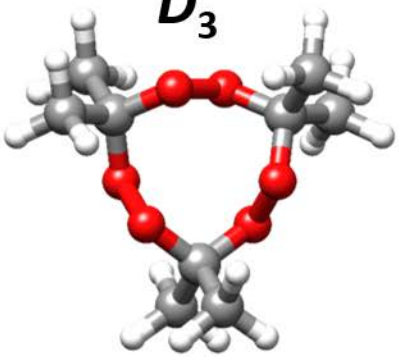

D_3

ΔE= 0 kJ/mol

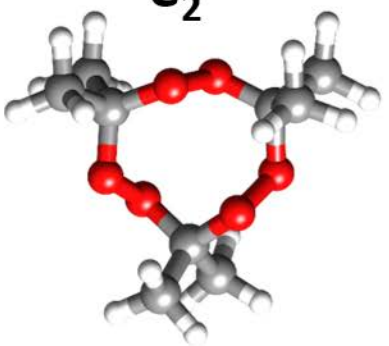

C_2

ΔE= 7.6 kJ/mol

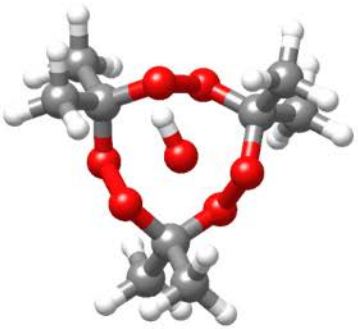

TATP-H_2O I

ΔE= 0 kJ/mol

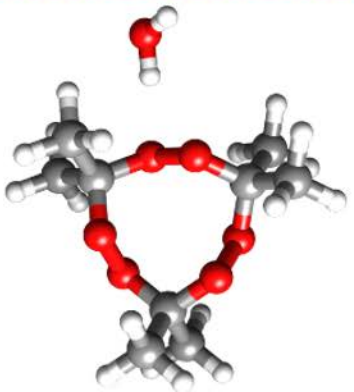

TATP-H_2O II

ΔE= 2.6 kJ/mol

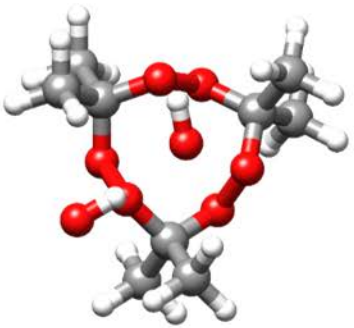

TATP-$(H_2O)_2$ I

ΔE= 0 kJ/mol

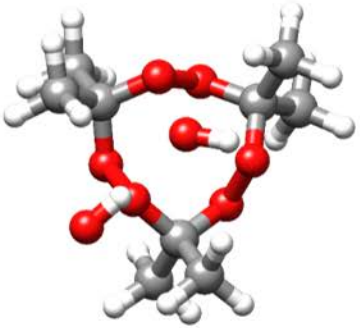

TATP-$(H_2O)_2$ II

ΔE= 0.5 kJ/mol

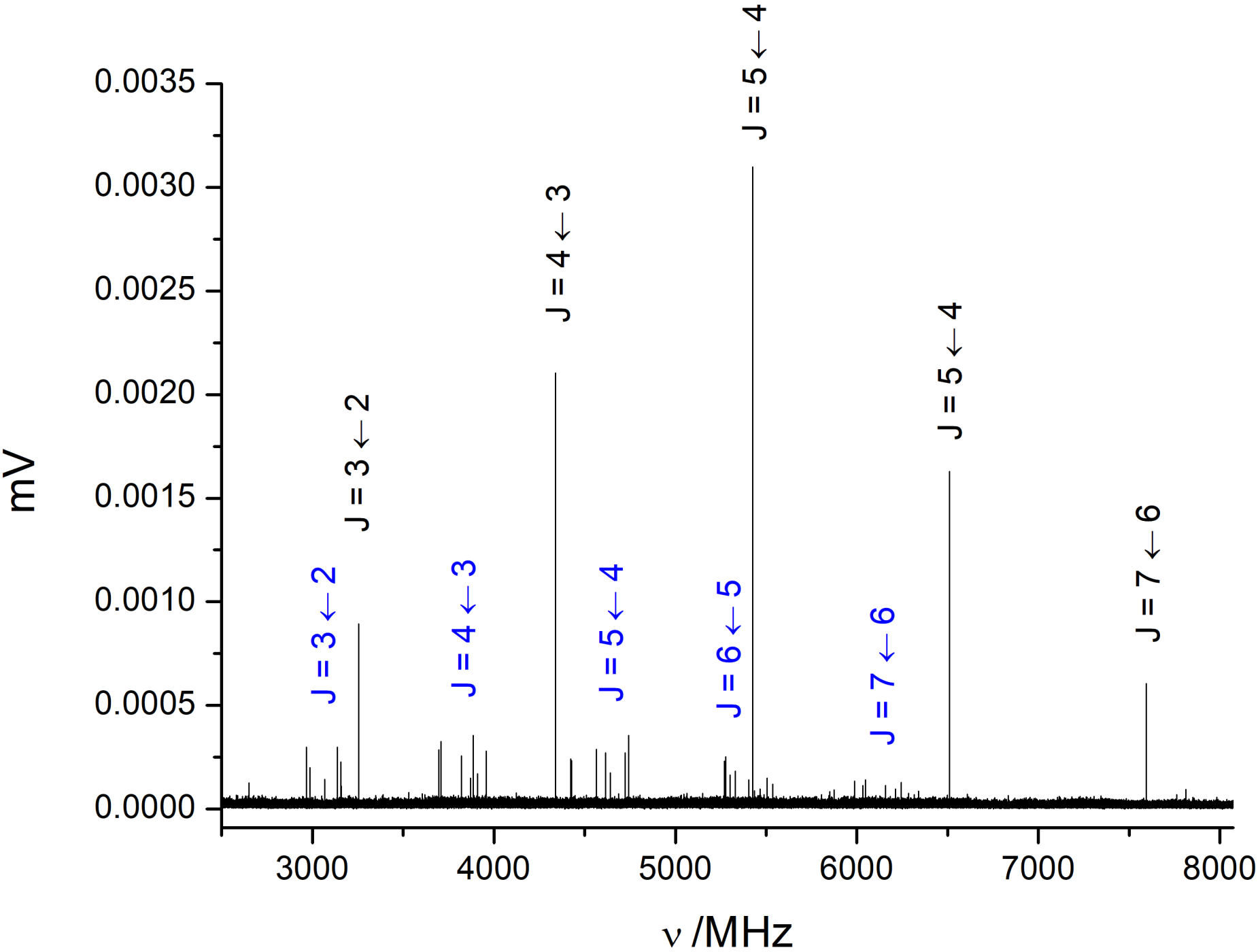
0.0035
0.0030
0.0025
0.0020
0.0015
0.0010
0.0005
0.0000
mV
3000
4000
5000
6000
7000
8000
ν /MHz
J = 3 ← 2
J = 3 ← 2
J = 4 ← 3
J = 4 ← 3
J = 5 ← 4
J = 5 ← 4
J = 6 ← 5
J = 7 ← 6
J = 5 ← 4
J = 7 ← 6

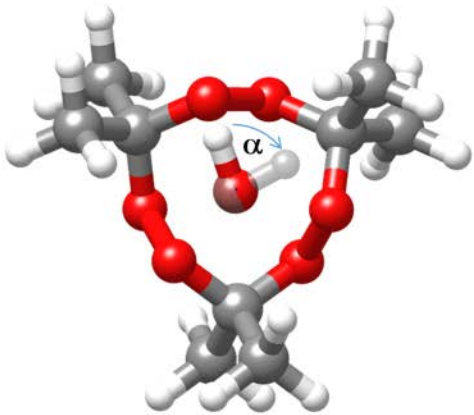

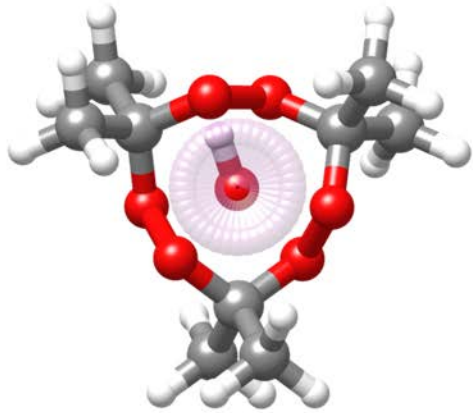

Equilibrium Structure
Asymmetric top

	DFT	MP2
A_e/MHz	545.4	549.3
B_e/MHz	544.8	548.8
C_e/MHz	437.0	440.3

Effective Structure
Symmetric top

	DFT	MP2
A_0/MHz	545.1	549.1
B_0/MHz	545.1	549.1
C_0/MHz	437.3	440.6

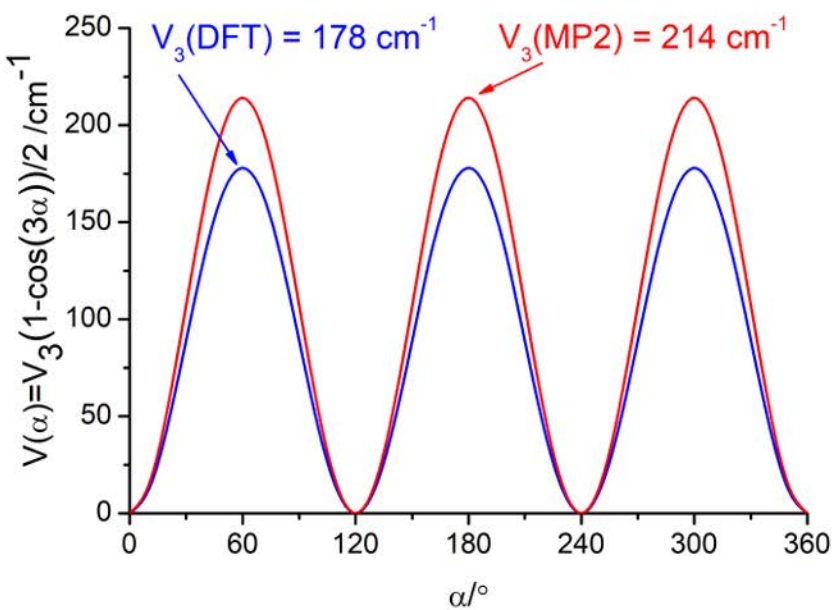

r_s

$|c_{O_w}| = 3.0905(4)$ Å

$|c_{H_{w1}}| = 2.0216(7)$ Å

$|c_{H_{w2}}| = 3.4283(4)$ Å

r_0

$r(O_w \cdots x_1) = 3.3381(6)$ Å

$r(O_w \cdots O_{TATP}) = 3.210(1)$ Å

$r(H_{w1} \cdots O_{TATP}) = 2.424(1)$ Å

$r(H_{TATP} \cdots O_w) = 2.656(1)$ Å

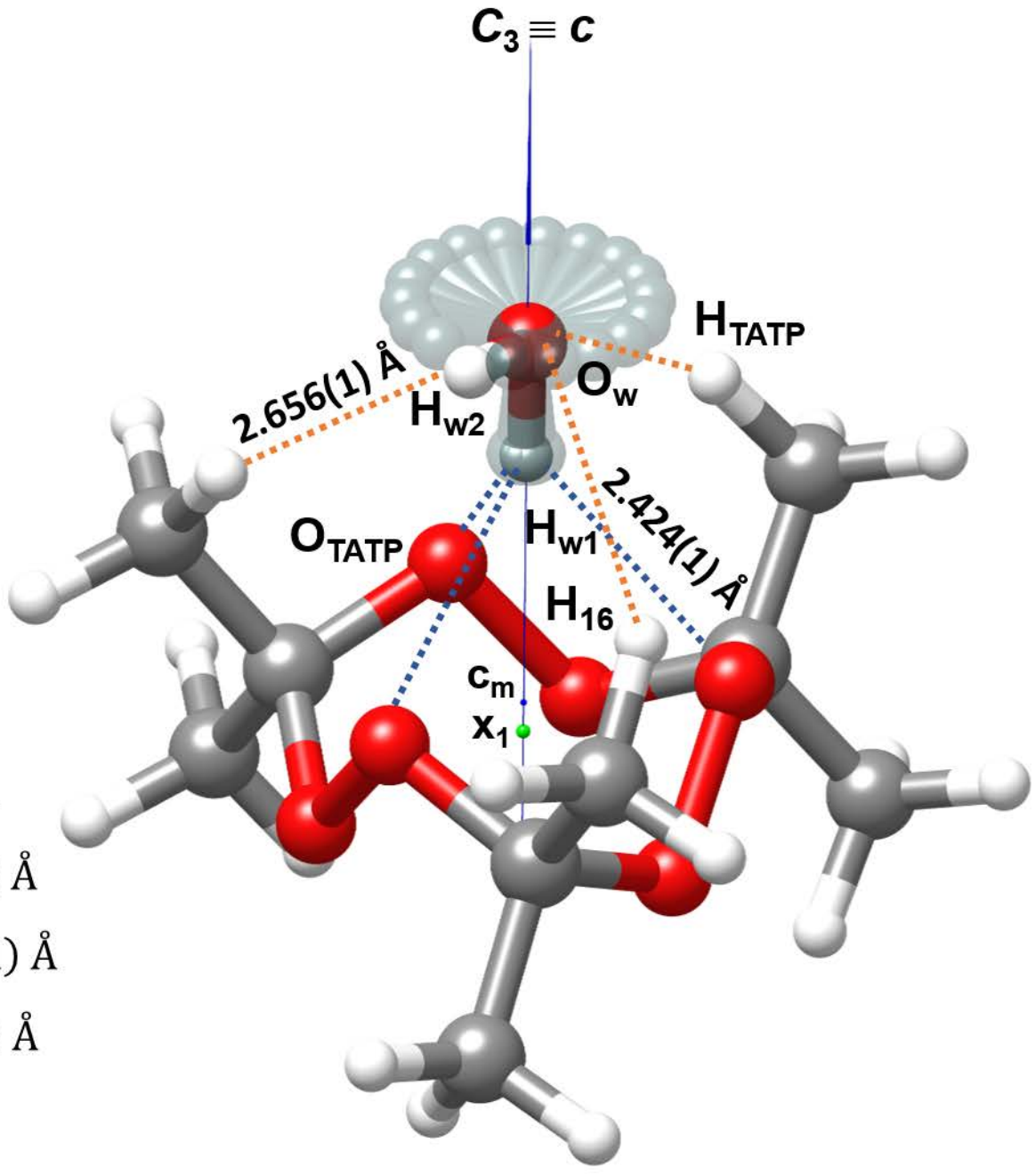

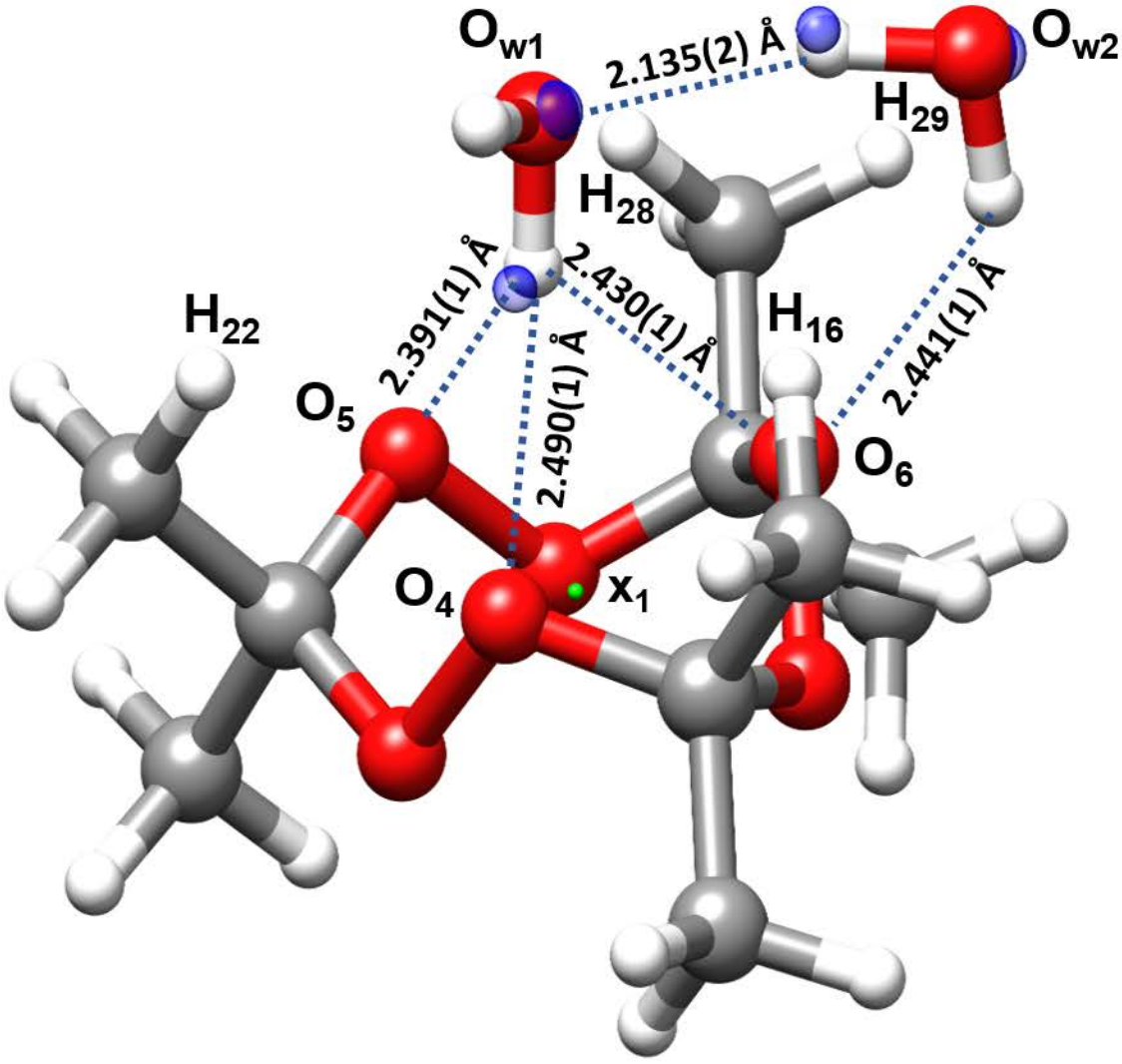

$r(\mathrm{O_{w1}} \cdots \mathrm{x_1}) = 3.290(1)$ Å

$r(\mathrm{O_{w1}} \cdots \mathrm{O_{w2}}) = 3.076(2)$ Å

$r(\mathrm{O_{w1}} \cdots \mathrm{O_4}) = 3.253(1)$ Å

$r(\mathrm{O_{w1}} \cdots \mathrm{O_5}) = 3.179(1)$ Å

$r(\mathrm{O_{w1}} \cdots \mathrm{O_6}) = 3.128(1)$ Å

$r(\mathrm{O_{w2}} \cdots \mathrm{O_6}) = 3.162(1)$ Å

$r(\mathrm{H_{16}} \cdots \mathrm{O_{w1}}) = 2.658(1)$ Å

$r(\mathrm{H_{22}} \cdots \mathrm{O_{w1}}) = 2.759(1)$ Å

$r(\mathrm{H_{28}} \cdots \mathrm{O_{w1}}) = 2.534(1)$ Å

$r(\mathrm{H_{16}} \cdots \mathrm{O_{w2}}) = 2.826(1)$ Å

$r(\mathrm{H_{29}} \cdots \mathrm{O_{w2}}) = 3.008(1)$ Å

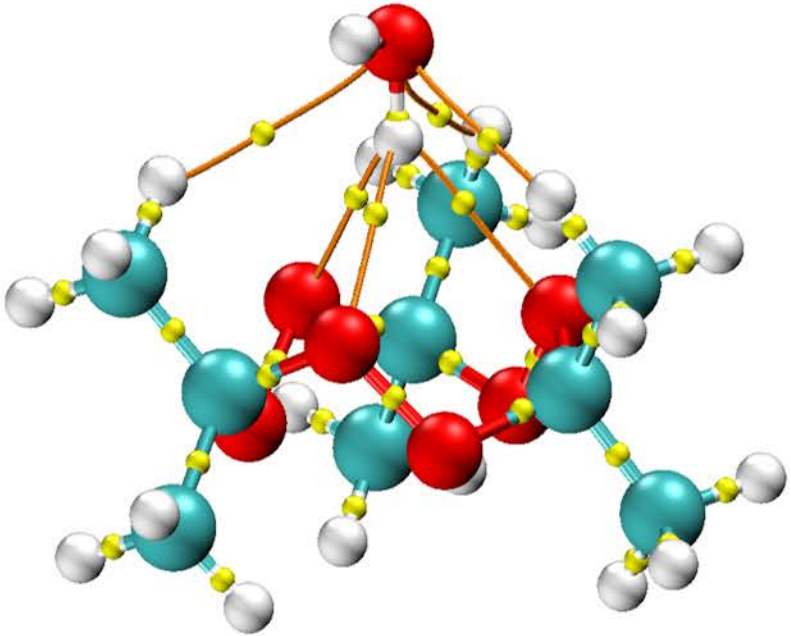

$E_{HB}(O_w\text{-}H\cdots O_{TATP})$=8.3-9.2 kJ/mol

$E_{HB}(C\text{-}H\cdots O_w)$=4.8-5.7 kJ/mol

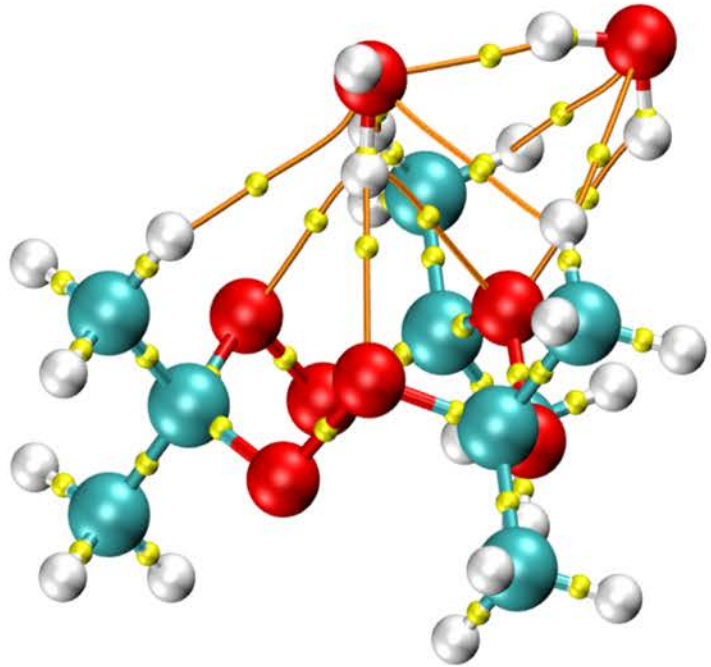

$E_{HB}(O_{w2}\text{-}H\cdots O_{w1})$=19.2 kJ/mol

$E_{HB}(O_{w1}\text{-}H\cdots O_{TATP})$=12.1-12.6 kJ/mol

$E_{HB}(O_{w2}\text{-}H\cdots O_{TATP})$=13.7 kJ/mol

$E_{HB}(C\text{-}H\cdots O_{w1})$=5.9-7.0 kJ/mol

$E_{HB}(C\text{-}H\cdots O_{w2})$=3.4-4.6 kJ/mol

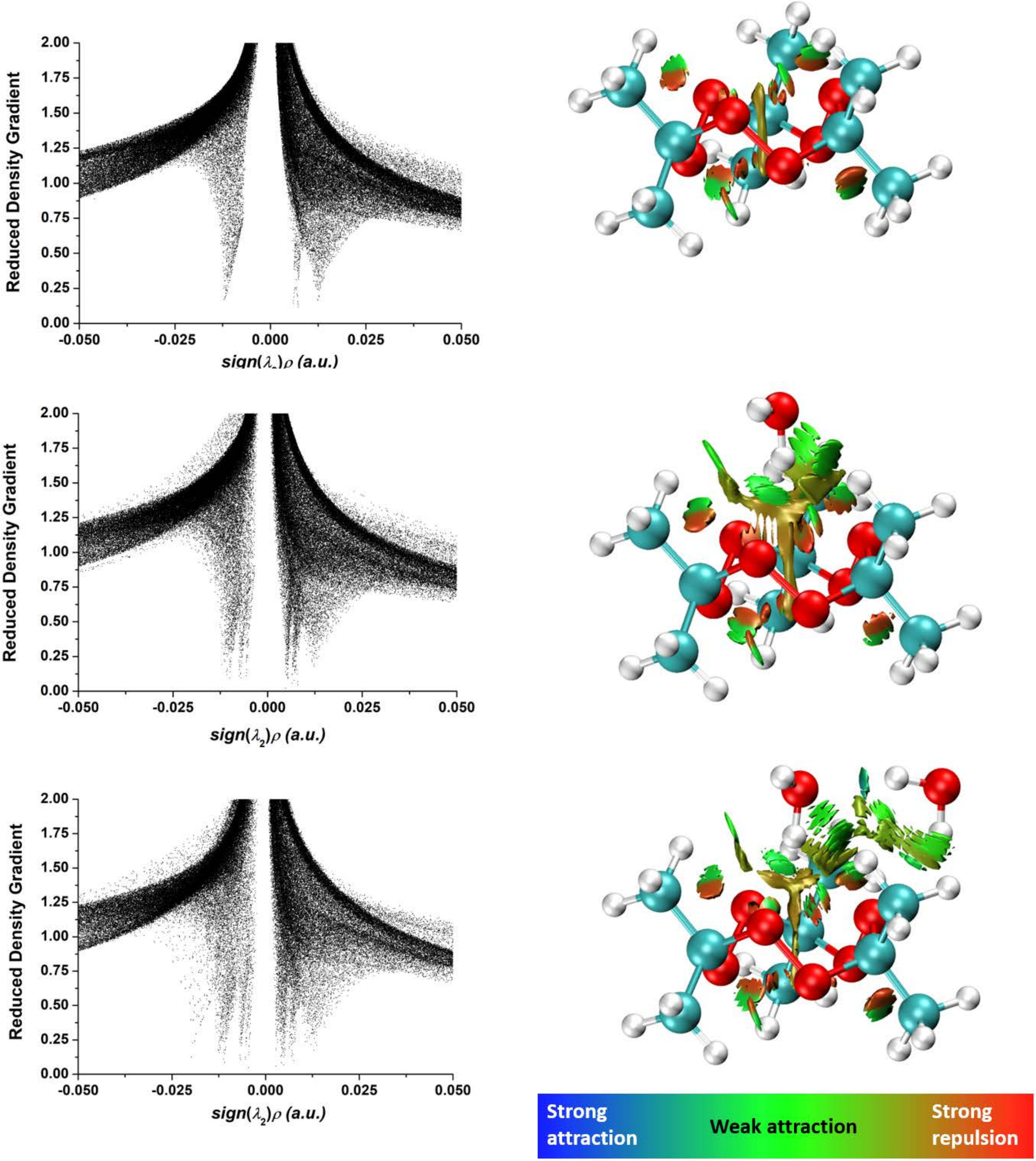

Reduced Density Gradient
2.00
1.75
1.50
1.25
1.00
0.75
0.50
0.25
0.00
-0.050
-0.025
0.000
0.025
0.050
sign(λ2)ρ (a.u.)
Reduced Density Gradient
sign(λ2)ρ (a.u.)
Reduced Density Gradient
sign(λ2)ρ (a.u.)
Strong attraction
Weak attraction
Strong repulsion